

DFT+DMFT study of spin-charge-lattice coupling in covalent LaCoO₃

Hyowon Park^{1,2}, Ravindra Nanguneri^{1,3}, Anh T. Ngo²

¹*Department of Physics, University of Illinois at Chicago, Chicago, IL 60607, USA*

²*Materials Science Division, Argonne National Laboratory, Argonne, IL, 60439, USA*

³*Department of Chemistry, Brown University, Providence, RI 02912, USA*

(Dated: May 12, 2020)

We study energetics and the nature of both homogeneous and mixed spin (MS) states in LaCoO₃ incorporating structural changes of the crystal volume expansion and the Co-O bond disproportionation (BD) during the spin-state transition using the density functional theory plus dynamical mean field theory (DFT+DMFT) method. DFT+DMFT predicts that energetics of both excited spin states are almost the same while DFT+U calculations of the same structures energetically favor the MS states and produce various metastable solutions whose energetics depend sensitively on final spin states. Within DFT+DMFT, the homogeneous spin state in the expanded crystal volume shows the multiconfigurational nature with non-negligible occupancy probabilities of both high spin (HS) and low spin (LS) states along with d^6 and d^7 charge configurations indicating the dynamically fluctuating nature of spin and charge states due to the Co-O covalency. The nature of the MS state under the BD structure reveals that Co sites with the long Co-O bonds develop a Mott insulating state and favor HS with a d^6 configuration, while more covalent Co sites with the short Co-O bonds occupy more LS states with a d^7 configuration and behave as a band insulator, as a result, charge ordering is induced in the BD structure from the spin-state ordering. We also find that both energetics and electronic structure sensitively depend on the Co-O covalency effect, which can be tuned by changing the double counting potential and the resulting d -occupancy (N_d), and N_d close to 6.7 is consistent with the nature of the spin-state transition. Our results show that structural changes during the spin-state transition can play an important role in understanding energetics and electronic structure of LaCoO₃.

I. INTRODUCTION

Transition metal oxides exhibit complex and rich phase diagrams arising from the strongly correlated nature of spin, charge, orbital, and lattice degrees of freedom¹. LaCoO₃ has been known for the spin-state transition of partially filled d orbitals in a Co ion. At very low temperatures, LaCoO₃ is a non-magnetic insulator with the low spin (LS) state. As the temperature is elevated above 90K, the magnetic susceptibility changes to a Curie-Weiss form indicating that paramagnetism dominates with higher spin states while retaining an insulating behavior². The spin-state transition can be explained based on the atomic multiplet structure of the Co d orbital, namely from the $|S_z|=0$ LS ground state to $|S_z|=1$ intermediate spin (IS) or $|S_z|=2$ high spin (HS) state. Various experimental results have been used to interpret the higher spin state as either IS³⁻⁶ or HS^{7,8}. The MS of LS and HS has been also suggested to explain other experimental measurements⁹⁻¹³. Despite extensive experimental works, the nature of excited spin-states has not been clarified yet.

The spin-state transition in LaCoO₃ occurs since the Hund's coupling tends to maximize the spin and excite electrons from t_{2g} to e_g orbitals by overcoming the crystal field splitting between them. Here, the interplay between electron and lattice degrees of freedom plays an important role as the e_g orbital occupation increases the Co-O bond-length to reduce the repulsive Coulomb interaction of electrons between Co and O ions. This structural change also gives the positive feedback since the reduction of the crystal-field splitting can favor the spin-

state transition. This strong electron-lattice coupling has been measured experimentally by the anomalous lattice expansion arising due to the Co-O bond-length elongation at the spin-state transition¹⁴⁻¹⁷. Several scenarios of local structural distortions due to the spin excitation have been proposed although clear experimental evidences have not been given yet. The Co-O bond-disproportionation (BD) with alternating the long bond (LB) site and the short bond (SB) site^{9,18} was suggested to accommodate MS with HS and LS. The Jahn-Teller distortion^{6,19} was also discussed possibly due to the IS state. The strong electron-lattice coupling has been also shown in the tensile-strained LaCoO₃ film promoting various competing orders including spin²⁰⁻²², charge²³, and orbital orderings²⁴.

Alongside experimental measurements, various theoretical scenarios based on first-principle calculations have been proposed to address this long-standing problem of the spin-state transition in LaCoO₃. Density functional theory (DFT)+U calculations have been predicting that excited spin-states including IS^{25,26} and MS^{27,28} states can be energetically stable. Dynamical mean field theory (DMFT) can capture the multi-configurational nature of a paramagnetic state fluctuating dynamically beyond DFT+U^{29,30}. Early DFT+DMFT studies computed the single-particle spectra with spin-state crossover³¹ comparable to the experimental X-ray absorption spectra⁴ and also studied effects of the pressure³² and the Co-O covalency³³ on the spin-state transition. Both the homogeneous spin excitation including the electronic entropy³⁴ and the mixed LS and HS solution without any structural distortions^{35,36} have been discussed as the possible origin

of the spin-state transition within DFT+DMFT. However, no DFT+DMFT studies have addressed yet both the nature and energetics of paramagnetic states with all possible structural changes in this material.

In this paper, we adopt the DFT+DMFT method to study both homogeneous and MS states by incorporating structural changes during the spin-state transition. We show that the DFT+DMFT energetics treating the multi-configurational nature of a paramagnetic state can be noticeably different from the static DFT+U solutions in which various meta-stable spin-states are possible. We also find that both structural changes and the Co-O covalency effect tuned by the double counting potential can strongly affect the electronic structure and energetics of spin-states in LaCoO₃. In the expanded crystal volume, the occupation probabilities of higher spin-states in the Co ion increase as Co *d* orbitals become more correlated. As temperature increases, DFT+DMFT can reproduce the insulator-to-metal transition, consistent with experiment, as the correlation in the Co ion becomes weaker. In the BD structure, the Co ion in the Co-O LB behaves as a Mott insulator with HS while the Co ion in the SB becomes a band insulator favoring LS. The charge ordering is also induced in the BD structure as the LB Co ion favors a *d*⁶ configuration while the SB Co ion occupies more *d*⁷ states. The charge-self-consistency in DFT+DMFT plays a role to reduce the charge ordering in the BD structure.

This paper is organized as follows. In Sec. II, the method used in this paper is explained in details. Sec. III A discusses the energetics of possible spin-state transition in LaCoO₃ comparing DFT+DMFT and DFT+U. The nature of the paramagnetic state treated in DFT+DMFT is shown in Sec. III B by computing the occupation probabilities of different spin-states. The origin of charge ordering driven by spin-state ordering in the BD structure is revealed in Sec. III C. Results of the density of states computed using DFT and DFT+DMFT for different structures and temperatures are shown in Sec. III D. The self-energy data are displayed in Sec. III E and the effect of the charge-self-consistency in DFT+DMFT is also discussed in Sec. III F. We summarize our paper with conclusions in Sec. IV.

II. METHOD

A. Structural relaxation

To study possible structural distortions during the spin-state transition, we first perform the structural relaxation by adopting the DFT+U method as implemented in the Vienna ab-initio simulation package (VASP) code^{37–40} using different spin-states as initial guess. The Perdew-Burke-Ernzerhof (PBE) functional⁴¹ is used for the exchange-correlation functional within DFT. The DFT+U convergence is achieved using the plane-wave energy cut-off of 600eV and the *k*-point

Structures	S.G.	Vol.[Å ³]	Co-O[Å]	Mom.[μ _B]	<i>N_d</i>
S1(LS)	<i>R3c</i>	56.40	1.95	0	7.1
S2(IS)	<i>R3c</i>	57.98	1.97	2.2	7.1
S3(MS) Co1	<i>R3</i>	57.98	1.99	3.0	6.9
S3(MS) Co2	<i>R3</i>	57.98	1.94	0.3	7.2

TABLE I. The structural information of LaCoO₃ relaxed structures obtained using DFT+U with U=6eV and J=0.9eV. Three different structures are obtained by relaxing with different magnetic moments and they are denoted as S1 (relaxed with LS), S2 (relaxed with IS), and S3 (relaxed with MS). The space group (S.G.), the crystal volume per formula unit, the Co-O bond length, magnetic moments, and the *d*-occupancy (*N_d*) are given in this table.

mesh of 8×8×8. The convergence of the structural relaxation is achieved if the atomic forces of all ions are smaller than 0.01eV/Å. Within DFT+U, we use the on-site Hubbard interaction U=6eV, which is obtained using the constraint DFT method³³, and the Hund's coupling J=0.9eV. Although the ground-state of LaCoO₃ is paramagnetic, DFT+U relaxation calculations are performed with the ferromagnetic configuration since correlations are included by imposing a long-range magnetic order in DFT+U.

LaCoO₃ is a rhombohedral structure with the *R3c* symmetry containing two Co ions per unit cell. The experimental crystal volume *V* is 56.0Å³ per formula unit at low temperatures¹⁷. We find that the DFT+U relaxation calculation with the PBE functional converging to LS produces the volume *V* of 56.40Å³ per formula unit with the Co-O bond-length *a* ~ 1.95Å (S1 structure in Table. I), while the IS state (magnetic moment=2.2μ_B) results in the 2.7% volume expansion resulting *V* ~ 57.98Å³ per formula unit and *a* ~ 1.97Å (S2 structure in Table. I). The HS structure converged to a more expanded volume but the total energy is much higher than either LS or IS one, therefore we do not consider the HS structure in this paper. Interestingly, the MS imposing HS to one Co ion and LS to the other Co ion within the unit-cell produces the BD structure by lowering the crystal symmetry from *R3c* to *R3* (S3 structure in Table.I). The crystal volume *V* is similar to the IS volume (*V* ~ 57.98Å³) and the HS site (magnetic moment=3μ_B) becomes a Co-O LB site with *a* ~ 1.99Å and the LS site (magnetic moment=0.3μ_B) is the SB with *a* ~ 1.94Å, resulting in the bond-length difference δ*a* ~ 0.05Å. The *d*-occupancy (*N_d*) for relaxation results in all structures are close to *d*⁷ (leaving one hole in surrounding oxygen atoms) although the nominal *d*-occupancy is *d*⁶ for LaCoO₃. This is due to the strongly covalent nature of the Co-O bonding in LaCoO₃. The summary of the relaxed structure information is given in Table I.

B. DFT+DMFT

Using LS, IS, and MS structures (denoted as S1, S2, and S3 in Table I) obtained from DFT+U relaxations, we employ a charge-self-consistent DFT+DMFT method^{42,43} to study the nature and energetics of the spin-state transition. The DFT+DMFT method is implemented using the maximally localized Wannier functions (MLWFs)^{44,45} as localized orbitals. First, we solve the non-spin-polarized Kohn-Sham (KS) equation within DFT using the VASP code. Then, we construct Co $3d$ and O $2p$ orbitals using MLWFs to represent the hybridization subspace for solving DMFT equations. The Co-O covalency effect can be treated within DMFT by including both d and p orbitals in the hybridization subspace. The $p-d$ Hamiltonian of the MLWF basis is constructed from the DFT bands in the hybridization energy window of 11eV. Then, the correlated subspace of Co $3d$ orbitals is treated using the continuous time quantum Monte Carlo (CTQMC)^{46,47} impurity solver by solving the DMFT self-consistent equations. The Hubbard U is 6eV and the Hund's coupling J is 0.9eV within the Co $3d$ shell while we compute the local self-energy for Co $3d$ orbitals within DMFT calculations for the study of spin-state transitions. Within DMFT, we use temperatures from 100K to 1000K to study the temperature effect on the spectral function while 300K is used for most calculations unless specified otherwise. Here, both U and J are parameterized by Slater integrals (F^0 , F^2 , and F^4), namely $U=F^0$ and $J=(F^2 + F^4)/14$. The Coulomb interaction matrix elements with only density-density types are considered in CTQMC while the spin-flip and pair-hopping terms are neglected. Also, we chose the cartesian axes of Wannier orbitals to be aligned along the Co-O bonds so that the off-diagonal terms in the d -Hamiltonian can be much smaller (even zeros) than the on-site terms (see Appendix A). Therefore, the off-diagonal terms in the DMFT hybridization function can be also ignored within CTQMC.

The charge-self-consistency in DFT+DMFT can be achieved by updating the charge density using the DMFT local Green's function while the DMFT loop is converged. The KS equation is solved again using the updated charge density and the new $p-d$ Hamiltonian is constructed using the updated MLWFs obtained from the KS solutions. The full charge-self-consistent DFT+DMFT loop is continued until both the charge density, the DMFT Green's function G^{loc} , and the DMFT self-energy Σ^{loc} are converged. More details of the DFT+DMFT implementation combining the projected augmented wave method in the DFT part and the formula for the charge update can be found in Ref. 42. For the precise convergence, the energy cut-off of 600eV and the k -point mesh of $8 \times 8 \times 8$ are used for DFT loops and a more dense k -point mesh of $30 \times 30 \times 30$ is used within the hybridization window of Wannier orbitals for DMFT loops.

Once the DFT+DMFT self-consistency loop is converged, the total energy E is computed using the follow-

ing formula:

$$E = E^{DFT}[\rho] + \frac{1}{N_{\mathbf{k}}} \sum_{\mathbf{k}, i \in W} \epsilon_{i\mathbf{k}} \cdot (n_{i\mathbf{k}} - n_{i\mathbf{k}}^0) + E^{POT}[G^{loc}] - E^{DC}[N_d] \quad (1)$$

where E^{DFT} is the DFT energy computed using the charge density ρ obtained within DFT+DMFT, $\epsilon_{i\mathbf{k}}$ is the DFT eigenvalues, $n_{i\mathbf{k}}$ is the diagonal part of the DMFT occupancy matrix element with the KS band index i and the momentum \mathbf{k} , W is the energy window for the hybridization subspace, and $n_{i\mathbf{k}}^0$ is the DFT occupancy matrix element with the KS band i and the momentum \mathbf{k} . The potential energy E^{POT} within DMFT is given by the Migdal-Galinski formula: $E^{pot} = \frac{1}{2} \text{Tr}[\Sigma^{loc}(i\omega) \cdot G^{loc}(i\omega)]$.

The double counting (DC) energy, E^{DC} needs to be defined for beyond-DFT methods such as DFT+DMFT and DFT+U since the potential energy treated in the correlated subspace is already accounted as the part of the DFT energy and it needs to be subtracted from the total energy formula. Various DFT+DMFT calculations suggest that the DC potential, $V^{DC} (= \partial E^{DC} / \partial N_d)$, smaller than the conventionally used fully-localized-limit (FLL) form⁴⁸ can produce better agreements of energetics^{42,49}, the metal-insulator transition⁵⁰⁻⁵², and the $p-d$ orbital splitting^{50,52,53} of oxides compared to experiments. Recently, it has been also shown that the more exact form of V^{DC} within DFT+DMFT can be derived⁵³ and the exact V^{DC} value can be close to the nominal DC form, in which the d -occupancy, N_d , in the FLL formulae is replaced to the nominal d -occupancy, N_d^0 (d^6 in the LaCoO₃ case). More detailed discussions about different formula of double counting corrections are given in Appendix B.

In this paper, we propose the following form of V^{DC} to allow the change between the FLL form and the nominal DC form by replacing N_d to \overline{N}_d :

$$E^{DC} = \frac{U}{2} \cdot \overline{N}_d \cdot (\overline{N}_d - 1) - \frac{J}{4} \cdot \overline{N}_d \cdot (\overline{N}_d - 2) \quad (2)$$

$$V^{DC} = U \cdot (\overline{N}_d - \frac{1}{2}) - \frac{J}{2} \cdot (\overline{N}_d - 1) \quad (3)$$

where U and J are the same paramters which are defined above for the Slater-type interaction, $\overline{N}_d = N_d - \alpha$ where N_d is the d -occupancy obtained self-consistently at each correlated site, and α is a parameter which can be tuned for obtaining different E^{DC} and V^{DC} values from the conventional FLL form. Our V^{DC} formula can be derived from E^{DC} ($V^{DC} = \partial E^{DC} / \partial N_d$) and allow site-dependent DC potentials. Our modified V^{DC} form can recover the conventional FLL DC form by setting $\alpha=0$. By increasing α , V^{DC} approaches to the nominal V^{DC} value as \overline{N}_d becomes N_d^0 ($\alpha = N_d - N_d^0$). One should note that changing V^{DC} with different α values can also tune the $p-d$ covalency effect by effectively shifting the d orbital level. For example, a smaller V^{DC} potential than the FLL DC potential will make the d orbital level higher and the covalency effect weaker, resulting in a reduced N_d value. The $p-d$ energy separation predicted by DFT or

DFT+U with the FLL DC can be usually overbound and the physical role of α is to avoid this overbinding effectively by increasing the $p-d$ energy separation. In this paper, We studied the effect of the Co-O covalency on energetics and the nature of spin states in LaCoO₃ by changing V^{DC} potentials using different α values.

III. RESULTS

A. Energetics of spin-state transition: DFT+DMFT vs DFT+U

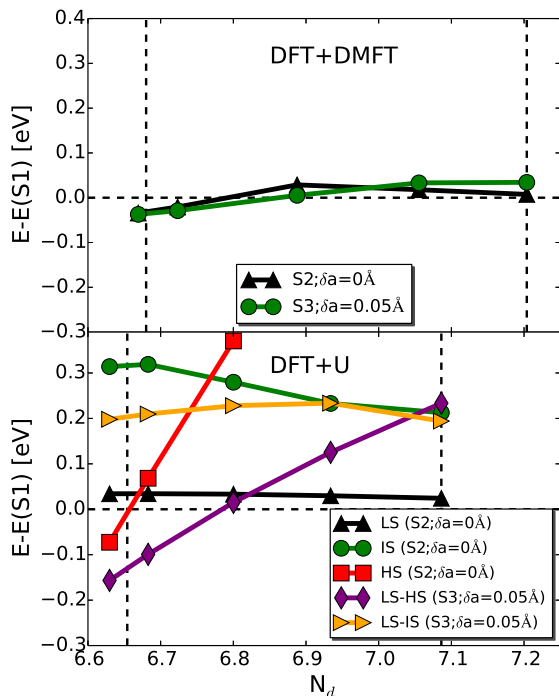


FIG. 1. Total energy differences between excited spin-state structures (S2 and S3) and the LS structure (S1) in LaCoO₃ computed using DFT+DMFT (top panel) and DFT+U (bottom panel) as a function of N_d tuned by different α values in V^{DC} (Eq. 3). The S3 structure ($\delta a=0.05\text{\AA}$) can incorporate the mixed spin-states between two Co ions in the unit cell. The left vertical dashed line represents the N_d value obtained from the nominal DC formulae while the right dashed line shows N_d obtained using the FLL DC formulae. Both DFT+DMFT and DFT+U methods use the same correlated orbitals (MLWFs) with the same interaction parameters ($U=6\text{eV}$ and $J=0.9\text{eV}$). Temperature is 300K within DMFT calculations.

Here, we begin by showing the effect of different DC potential (V^{DC}) values on the energetics of spin-states in LaCoO₃ computed using DFT+DMFT (Fig.1 top panel) and DFT+U (Fig. 1 bottom panel). The x -axis shows N_d values obtained by changing V^{dc} in Eq. 3 using different α values, namely $\alpha=0, 0.2, 0.4, 0.6,$ and 0.7 . Two vertical dashed lines indicate the N_d values obtained using

the FLL DC formulae (the right line) and the nominal DC formulae (the left line). The calculations with the FLL DC ($\alpha=0$) converge to $N_d \sim 7.2$ for DFT+DMFT and 7.1 for DFT+U while those with the nominal DC result in $N_d \sim 6.68$ for DFT+DMFT and 6.65 for DFT+U. The y -axis indicates the total energy difference between the expanded volume structures (S2 and S3; $V \sim 57.98\text{\AA}^3$) accompanying excited spin-states and the S1 structure ($V \sim 56.4\text{\AA}^3$). Here, DFT+U energies are computed by adopting the MLWFs as correlated orbitals consistently with DFT+DMFT calculations, therefore the difference between DFT+DMFT and DFT+U results is attributed purely to the dynamical correlation effect beyond DFT+U. Also, the previous study of DFT+U calculations using different choices of orbitals (MLWFs vs projectors) has shown that results of the structural phase diagram of nickelates are almost the same as long as the same U and J values are used⁵⁴. Therefore we expect that the energetics results reported here will not depend much on the choice of correlated orbitals.

The energetics obtained using two methods show noticeable differences depending on N_d (the Co-O covalency effect). The DFT+DMFT energy difference between two expanded volume structures (S2($\delta a=0\text{\AA}$) and S3($\delta a=0.05\text{\AA}$)) is much smaller (maximally 20meV) than the DFT+U energy difference while DFT+U solutions converge to various meta-stable states for a given structure (LS, IS, and HS for S2 and LS-HS and LS-IS for S3) and the DFT+U energy depends sensitively on N_d and spin-states. This difference in energetics arises since the spin-state within DFT+DMFT is described as a multi-configurational state with a mixture of various spin states showing smooth crossover (see Fig. 2) while the DFT+U solution is based on a single-determinant form and produces meta-stable states depending on given structure and N_d .

Within DFT+DMFT, the S2 structure (triangular dot) is more stable when $N_d > 7.0$ and the LS state is dominant while the S3 BD structure (circular dot) becomes stable when the spin-state transition to LS-HS occurs ($N_d < 7.0$). Two structures become energetically almost the same when N_d is further reduced ($N_d \sim 6.7$) since the energy of the S2 structure gets lowered as HS is more excited at smaller N_d . The dependence of DFT+U energetics on N_d favors the MS (LS-HS) state although it behaves qualitatively similar to DFT+DMFT as LS with the S2 structure is stable when $N_d > 6.8$ and LS-HS with the S3 BD structure becomes rapidly stable when N_d is further reduced. The energy of HS with the S2 structure is also rapidly decreasing at smaller N_d as the Hund's coupling lowers the energy in the HS state. Within DFT+U, energetics of other meta-stable states including LS and LS-IS do not depend much on N_d while IS is not favored as N_d is reduced. Our calculations show that the spin-state transition from the S1 (LS) structure to excited spin-states with the expanded volume ($E-E(S1) < 0$) occurs when N_d becomes smaller (< 6.9 for DFT+DMFT and < 6.8 for DFT+U) than

the FLL DC result. This is consistent with the nominal V^{DC} result (the left vertical dashed lines; $N_d \sim 6.68$ for DFT+DMFT) and due to the fact that higher spin states are more excited at smaller N_d as will be shown in Fig. 2.

B. Nature of paramagnetic states

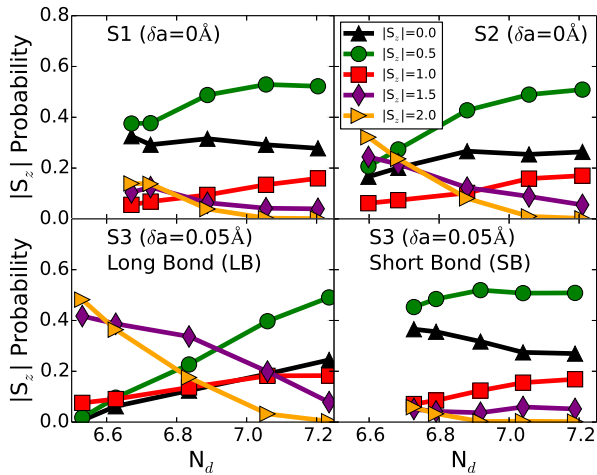


FIG. 2. The occupation probability of the spin $|S_z|$ state sampled using the CTQMC method within DFT+DMFT as a function of N_d for the S1 structure ($V = 56.40\text{\AA}^3$, upper left panel), the S2 structure ($V = 57.98\text{\AA}^3$, upper right panel), and the S3 structure with the long-bond (lower left panel) and the short-bond (lower right panel) sites.

Now we turn to the nature of paramagnetic states in LaCoO_3 obtained within DFT+DMFT. Fig. 2 displays the spin $|S_z|$ probabilities sampled using CTQMC as a function of N_d for different structures. The multi-configurational nature of the paramagnetic state treated in DFT+DMFT means that various $|S_z|$ states ($S_z = 0.0 \sim 2.0$) contribute to the solution. In all structures, the charge d^7 state with $|S_z| = 0.5$ and 1.5 is not negligible in addition to the nominal d^6 state with $|S_z| = 0, 1,$ and 2 , therefore LaCoO_3 is strongly covalent with the dynamically fluctuating nature of spin and charge states. When $N_d > 7.0$, LS with $|S_z| = 0$ and 0.5 has the highest probability for all structures, consistently with the fact that the S1 structure ($V = 56.40\text{\AA}^3$) is energetically stable. As N_d is reduced, LS is still dominant for the S1 structure while HS with $|S_z| = 1.5$ and 2 becomes more excited for the S2 structure ($V = 57.98\text{\AA}^3$). The nature of paramagnetic state in the S2 structure, which is energetically stable when $N_d < 6.7$, is characterized by a mixture of both LS and HS, fluctuating dynamically with non-negligible probabilities. The IS state ($|S_z| = 1.0$) is strongly suppressed for all structures. In the BD structure, HS with $|S_z| = 1.5$ and 2 becomes rapidly favored in the LB site as N_d is reduced while LS with $|S_z| = 0$ and 0.5 is always dominant in the SB site. These DFT+DMFT results of paramagnetic states ex-

hibiting the mixture of different spin states are distinct from the DFT+U results where meta-stable solutions of spin states are found.

C. Charge ordering induced by spin-state ordering

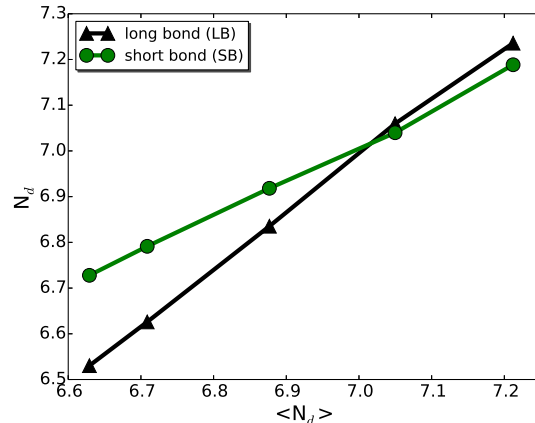


FIG. 3. The d -occupancy, N_d computed for both the long-bond and the short-bond sites in the S3 structure computed using DFT+DMFT as a function of the average $\langle N_d \rangle$ between two sites.

The strongly coupled spin and charge degrees of freedom also produce an intriguing rock-salt type charge ordering state induced from the MS state in the S3 structure. Fig. 3 shows that the DFT+DMFT charge in the LB site (triangular dots) gets smaller more rapidly than the SB charge (circular dots) as the average $\langle N_d \rangle$ becomes reduced (the overall Co-O covalency is reduced). This is because HS in the LB site favors the $|S_z| = 2$ with d^6 state while the $|S_z| = 0.5$ with d^7 state is dominant in the SB site as the Co-O covalency remains strong. This enhancement of charge ordering when $N_d < 6.9$ is also consistent with the rapid increase of the HS probability in the LB site as shown in Fig. 2. The experimental evidence of charge ordering with the concomitant spin-state ordering in LaCoO_3 has been reported in the tensile-strained film²³. The ground-state of this charge ordered LaCoO_3 is insulating and the nature of the LB site is a Mott insulator while the SB site is a band insulator due to the strong Co-O hybridization (see Fig. 8). This MS state in the S3 (BD) structure is somewhat reminiscent of the site-selective Mott physics occurring in nickelates in which the LB site is Mott insulating with the d^8 state while the SB site is a covalent insulator hybridized with O hole states as d^8L^2 .⁵⁵ Although charge ordering between two Ni sites in nickelates is not important to induce the insulating state in nickelates, charge ordering (~ 0.2) in LaCoO_3 is naturally induced from the spin-state ordering. Also, nickelates are negative charge-transfer insulators meaning that almost one electron is donated to each Ni ion from surrounding O ions while

the Co ion in LaCoO_3 favors a mixed-valence state with $N_d = 6.6 \sim 6.7$ as the charge transfer from the O hole is smaller than nickelates.

D. Density of states

In this subsection, we study the correlation, structure, $p-d$ covalency, and temperature effects on the spectral functions of LaCoO_3 . First, we show the density of states (DOS) computed using DFT paramagnetic calculations (no spin polarization) in Fig. 4. The DOS computed for the different structures shows very similar features. All structures are metallic without correlations and the S1 structure has slightly larger band-width than other structures due to the smaller crystal volume. Co t_{2g} states are all occupied below the Fermi energy Co e_g states are widely spread due to the strong mixing with the O p states. The LB and SB sites in the S3 structures exhibit the similar DOS without charge ordering ($N_d \sim 7.2$).

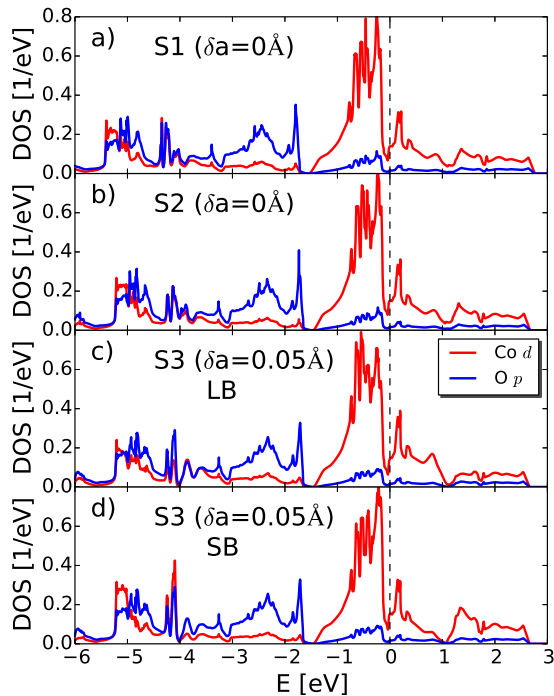


FIG. 4. The density of states computed for different structures of LaCoO_3 using DFT with the paramagnetic (no spin-polarization) symmetry. They are a) S1 ($V = 56.40 \text{ \AA}^3$), b) S2 ($V = 57.98 \text{ \AA}^3$), and S3 ($V = 57.98 \text{ \AA}^3$) structures with c) the Co-O long bond (LB) site and d) the short bond (SB) site.

Now, we include strong correlation effects in three structures (S1, S2, and S3) within DFT+DMFT and compute the DOS using the paramagnetic spin configuration in Fig. 5. We see dramatic changes of electronic structures due to correlation effects as well as the structural changes from the volume expansion and the Co-O bond disproportionation. The DOS in the S1 structure

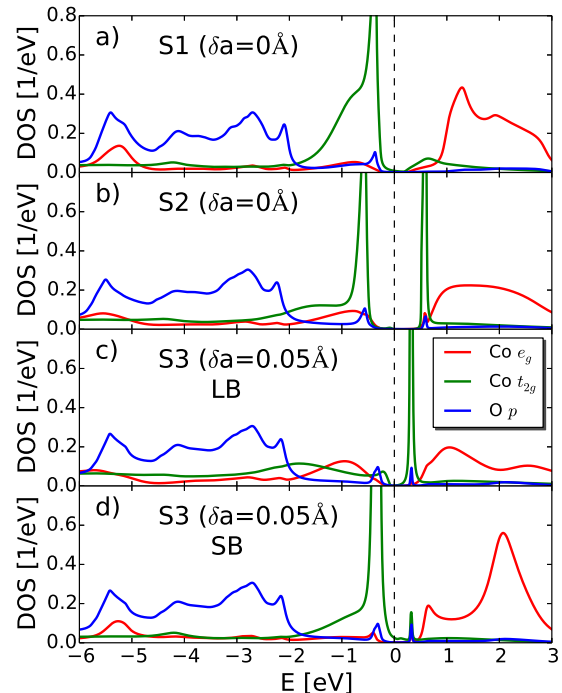


FIG. 5. The density of states obtained for different structures of LaCoO_3 using DFT+DMFT with $U=6\text{eV}$, $J=0.9\text{eV}$, and the DC parameter $\alpha = 0.7$ (Eq.3) resulting $N_d \sim 6.68$. Different structures are a) S1 ($V = 56.40 \text{ \AA}^3$), b) S2 ($V = 57.98 \text{ \AA}^3$), and S3 with c) the Co-O long bond and d) the short bond sites.

(Fig. 5 a) shows that the band gap is almost 0.6eV , which is consistent with the optical gap measurement⁵⁶. The t_{2g} state is almost occupied while the e_g state is mostly unoccupied, as expected for the LS state. As the volume is expanded, the spin-state transition to higher spins occurs continuously and the t_{2g} state begins to be unoccupied while more e_g orbitals are occupied (Fig.5 b). In the S1 structure, the major optical transition occurs from the Co t_{2g} valence band peak to the Co e_g conduction band peak while the transition between the same t_{2g} bands dominates in the S2 structure. Therefore, the position of the first major peak in the optical conductivity will be reduced as the crystal volume expands at higher temperature, which is consistent with the optical conductivity measurement in experiment. Moreover, our calculation shows that the S3 structure with the MS state produces the smaller gap than the S2 structure, therefore the optical gap can be further reduced as temperature is raised presumably with more populated MS states. The nature of the paramagnetic insulating state in the S2 structure is a strongly correlated band insulator driven by both the Co-O hybridization due to the covalency and the electron localization of the Co d orbitals due to increased HS states. This physics is captured in the imaginary part of the self-energy (see Fig.8 b) showing the emergence of the sharp pole outside the hybridization gap near the Fermi

energy. This paramagnetic insulating state is represented as a mixture of fluctuating HS and LS states (see Fig. 2) and it is distinct from the normal Mott insulator driven by the pure electron localization which is expected from the HS state in a d_6 configuration. In the S3 structure, the LB site becomes higher spin state with more unoccupied t_{2g} states while the SB site remains as LS with a similar gap size as the homogeneous LS gap. Here, the α value in V^{DC} (Eq. 3) is set to 0.7 resulting $N_d \sim 6.68$ for all structures. Different V^{DC} values will change the relative position of the O p peak from the Fermi energy as N_d is also varied. Our O p top peak position is located at -2eV when $N_d \sim 6.68$ and this peak position is consistent with the measured X-ray photo-emission spectra⁴ validating the α value we used.

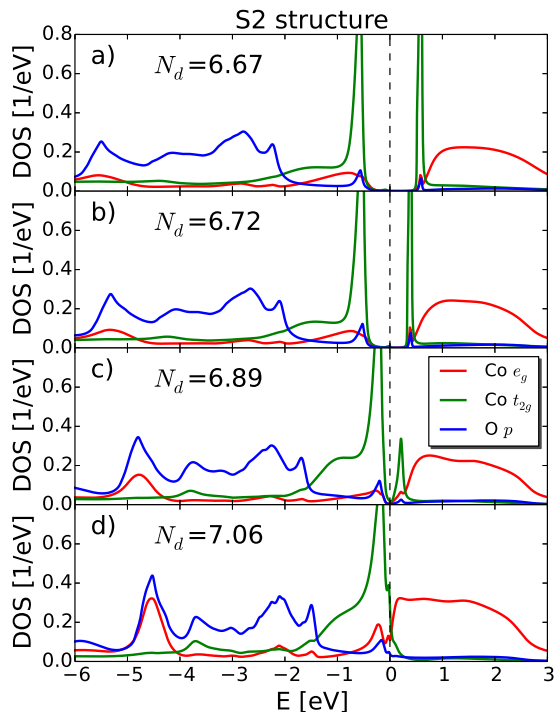


FIG. 6. The density of states computed using different α values in Eq. 3 within DFT+DMFT. The S2 structure is used. Different α values lead to distinct N_d results, namely a) $N_d = 6.67$ ($\alpha = 0.7$), b) $N_d = 6.72$ ($\alpha = 0.6$), c) $N_d = 6.89$ ($\alpha = 0.4$), and $N_d = 7.06$ ($\alpha = 0.2$). $U=6\text{eV}$ and $J=0.9\text{eV}$ are used within DMFT.

To clarify the role of the Co-O covalency (parametrized by N_d) on electronic structure, we show the DOS obtained using different α values for the S2 structure in Fig. 6. As the Co-O covalency is enhanced (N_d is increased), the O p peaks move closer to Co d states near the Fermi energy. As a result, the spectral gap becomes smaller due to the larger Co-O hybridization and the ground-state is eventually metallic when $N_d \sim 7.1$. Therefore, the insulator-to-metal transition occurs as the correlation in the Co ion is reduced due to the increased Co-O covalency and, at the same time, the spin states

are less excited as Co t_{2g} states are more occupied and e_g states are more unoccupied. This DOS result is also consistent with the occupation probability data of the S2 structure (Fig. 2 upper right panel) showing that the HS states ($|S_z| = 1.5$ and 2.0) are suppressed and the LS and IS states ($|S_z| = 0.0, 0.5,$ and 1.0) are gradually increasing as N_d increases. Our results suggest that the Co-O hybridization due to the covalency can play an important role in explaining the metal-insulator transition and the spin-state transition in LaCoO_3 .

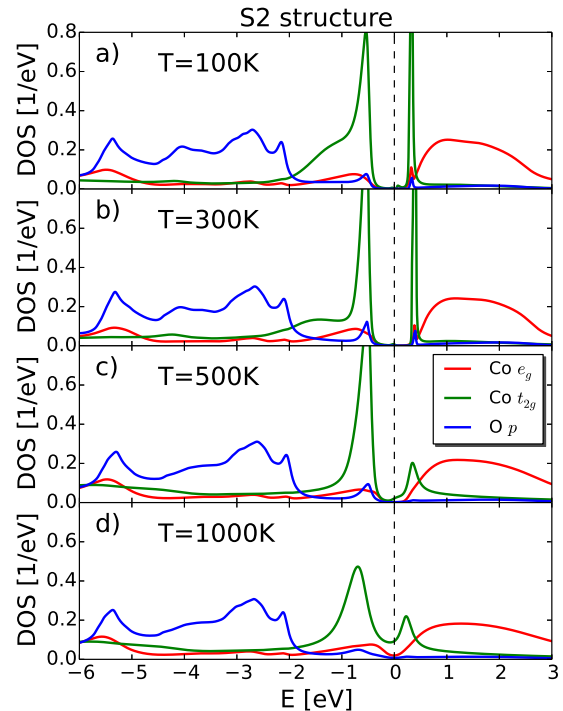


FIG. 7. The density of states computed for the S2 structure of LaCoO_3 using DFT+DMFT at different temperatures, namely a) $T = 100\text{K}$, b) 300K , c) 500K , and d) 1000K . $U=6\text{eV}$, $J=0.9\text{eV}$, and the double counting $\alpha = 0.6$ ($N_d \sim 6.7$) are used within DMFT.

Until now, our DFT+DMFT calculations have been performed at the fixed temperature ($\sim 300\text{K}$). Experimentally, LaCoO_3 also exhibits the insulator-to-metal transition as temperature is raised above near $T = 400\text{K}$ but the nature of this transition has not been clarified. To better understand the role of temperature on the metal-insulator transition in LaCoO_3 , we plot the DOS of LaCoO_3 at the fixed S2 structure and different temperatures (Fig. 7). The DOS data computed at both 100K and 300K show similar features although the spectral gap at 300K is slightly larger than one at 100K . The similarity of the DOS at low temperatures indicates that our spin-state calculations at 300K can be similarly reproduced at 100K (the experimental T_c of the spin-state transition). More importantly, the strong variation of the DOS and spin-states depending on structures in Fig. 5 means that the structural changes should be incor-

porated for the better description of electronic structure while temperatures are varied. Nevertheless, the spectral gap becomes smaller as temperature is raised above $500K$ and the Co t_{2g} state becomes the incoherent metallic state at around $1000K$.

E. Self-energy data

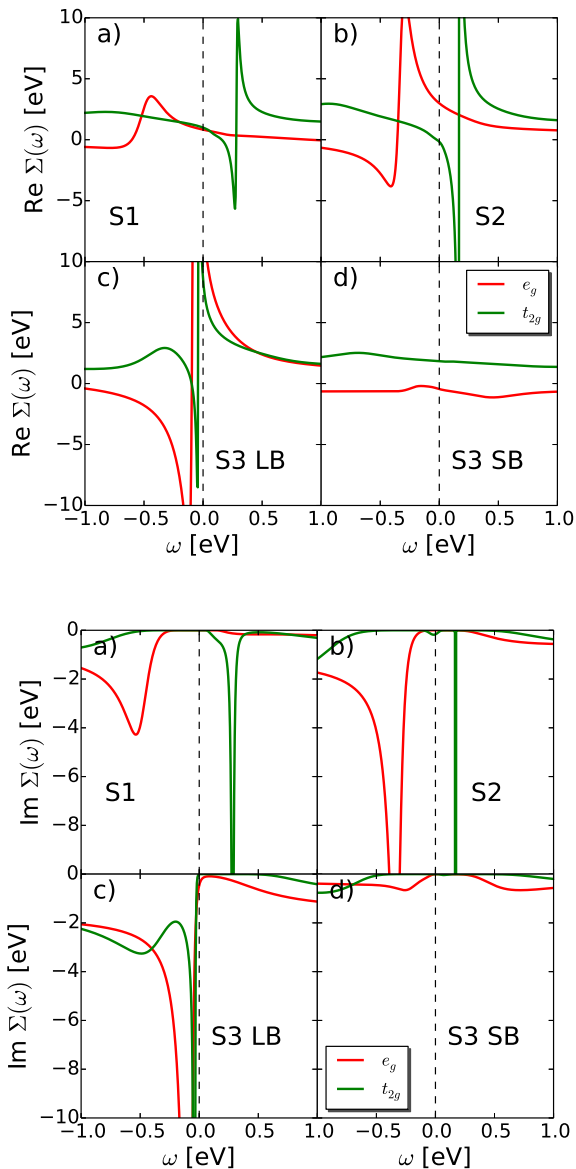


FIG. 8. The real part (top panel) and the imaginary part (bottom panel) of self-energy data computed for different structures in $LaCoO_3$, namely a) S1, b) S2, c) S3 Co-O long bond (LB), and d) S3 Co-O short bond (SB). $U=6eV$, $J=0.9eV$, and the double counting parameter $\alpha = 0.6$ ($N_d \sim 6.7$) are used.

To study the nature of insulating states occurring in

different structures, we show both the real part ($Re\Sigma$; Fig. 8 top panel) and the imaginary part ($Im\Sigma$; Fig. 8 bottom panel) of self-energies on the real axis, which are used to compute the DOS in Fig. 5. The S1 structure (Fig. 8a) exhibits rather small $Im\Sigma$ values in both e_g and t_{2g} orbitals when $\omega \sim 0$ while a sharp pole develops at $\omega \sim 300meV$ in the t_{2g} orbital for both real and imaginary parts. This diverging nature of the self-energy indicates Co d orbitals are still correlated even at the S1 structure with LS. This self-energy nature of LS is different from the typical band insulating nature of LS which is expected in a d^6 configuration. The nature of our insulating state is the correlated band insulator driven by both the Co-O hybridization and the electron correlation. The electron correlation is encoded in the sharp and narrow pole structure of the imaginary part of the self-energy developed outside the hybridization gap while the imaginary part of the self-energy is still zero at the Fermi energy. As the structure changes from S1 to S2 along with the volume expansion, the strength of poles becomes enhanced and the positions of the poles get close to the Fermi energy in both e_g and t_{2g} orbitals. This clearly shows that correlations are enhanced due to the increased higher spin probabilities (see Fig. 2) as the volume is expanded in $LaCoO_3$. The insulating nature of the S3 structure shows the “site-selective” Mott physics, as the Co-O LB site undergoes a Mott transition with the diverging self-energies at the Fermi energy while the SB site behaves as a band insulator with the small imaginary part and the flat real part of self-energies originated from the strong Co-O covalency.

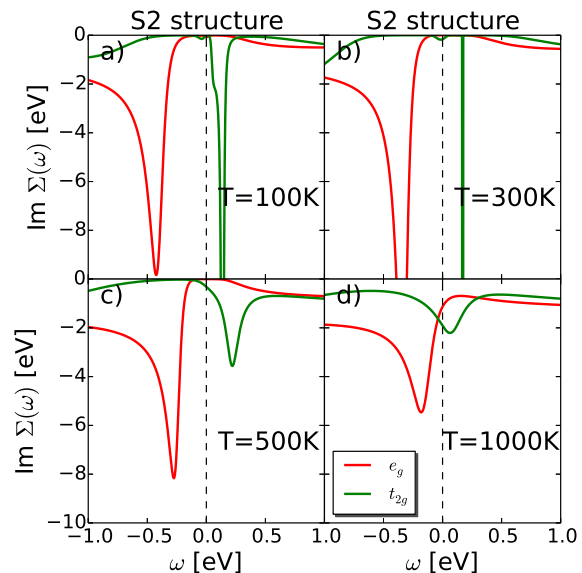


FIG. 9. The imaginary part of self-energy data computed for different temperatures at a fixed S2 structure in $LaCoO_3$, namely a) $T=100K$, b) $T=300K$, c) $T=500K$, and d) $T=1000K$. $U=6eV$, $J=0.9eV$, and the double counting parameter $\alpha = 0.6$ ($N_d \sim 6.7$) are used.

To understand the nature of the insulator-to-metal transition in LaCoO_3 as temperature is raised, we also plot the $Im\Sigma$ computed for the S2 structure as a function of temperature in Fig. 9. Results of $Im\Sigma$ at $T=100\text{K}$ show that poles are developed due to correlations at $\omega = -450\text{meV}$ for the e_g orbital and at $\omega = 150\text{meV}$ for the t_{2g} orbital. The strengths of these poles are enhanced at $T=300\text{K}$ as the S2 structure can occupy higher spin states due to the spin-state transition and electron localization can be enhanced at this temperature. This physics is different from the typical Mott insulator without any spin-state transition, in which the electron localization is usually stronger at lower temperature. As the temperature is raised even above 300K , the pole strengths are reduced and correlations become weaker for both e_g and t_{2g} orbitals resulting the metallic phase obtained in Fig. 7.

F. Charge-self-consistency effect

Finally, we show the charge-self-consistency effect in DFT+DMFT on the energetics and electronic structure in LaCoO_3 . Fig. 10 shows the energetics of spin-state transition in LaCoO_3 as a function of N_d comparing charge-self-consistent (top panel) and non-charge-self-consistent (bottom panel) DFT+DMFT calculations. Here, the non-charge-self-consistent calculation means that the charge density (ρ in Eq. 1) is fixed to the DFT one while the DMFT local Green's function (G^{loc} in Eq. 1) is obtained by converging DMFT self-consistent equations. As a result, the V^{DC} potential is fixed during the DFT+DMFT loop since the charge-density is not updated and V^{DC} is a function of the charge-density (N_d). Therefore, different N_d results in non-charge-self-consistent DFT+DMFT (bottom panel) are obtained by shifting the V^{DC} potential as data points are changed. However, in charge-self-consistent DFT+DMFT (top panel), V^{DC} is computed using the Eq. 3 with the self-consistently determined charge density (N_d) and the corresponding N_d is obtained from the DMFT Green's function.

The energetics of the S2 structure (homogeneous spin states) show the very similar behavior as a function of N_d between charge-self-consistent and non-charge-self-consistent calculations. In the case of the MS state for the S3 structure, non-charge-self-consistent DFT+DMFT energetics overestimate the tendency toward the spin-state ordering as the energy difference between the excited spin-state and the low-spin (S1) state becomes much lower ($\sim 150\text{meV}$) than the charge-self-consistent energetics ($\sim 30\text{meV}$) when $N_d \sim 6.7$. The energetics of the MS state also depend on N_d much sensitively in the non-charge-self-consistent case. Therefore, the main effect of charge-self-consistency in DFT+DMFT is to reduce the spin-state ordering effect in the S3 structure and the energetics between homogeneous and MS spin-states in the S2 and S3 structures become very close.

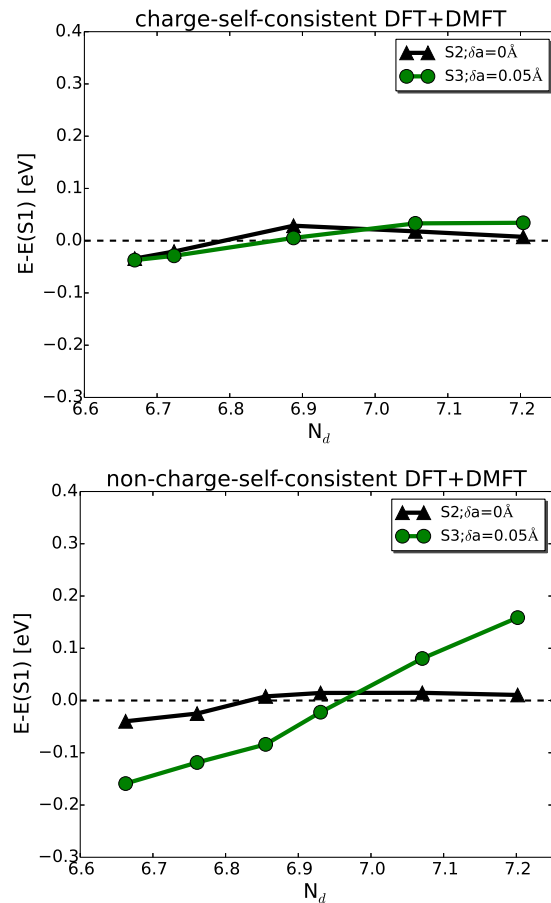


FIG. 10. Total energy differences between excited spin states (S2 and S3) and the low spin state (S1) in LaCoO_3 computed using both charge-self-consistent DFT+DMFT (top panel) and non-charge-self-consistent DFT+DMFT (bottom panel) as a function of N_d tuned by different V^{DC} potentials. The excited spin states incorporate the volume expansion with or without the Co-O bond-disproportionation ($\delta a=0.05\text{\AA}$ or 0\AA). $U=6\text{eV}$, $J=0.9\text{eV}$, and temperature $T=300\text{K}$ are used within DMFT.

To further investigate the effect of charge-self-consistency on electronic structure of LaCoO_3 , we display the d -occupancy, N_d in Fig. 11 obtained for both LB and SB sites in the S3 structure computed using charge-self-consistent DFT+DMFT (solid lines) and non-charge-self-consistent DFT+DMFT (dashed lines) as a function of the average N_d between two sites. Without the charge update (dashed lines), the N_d difference between two sites is more enhanced since the SB site occupies more d -orbitals while the LB site takes even less N_d compared to the charge-self-consistent results (solid lines) across different $\langle N_d \rangle$ values. Therefore, charge-self-consistency within DFT+DMFT reduces the tendency toward both spin-state and charge orderings between correlated Co sites, as a result, the energy difference between different excited spin-states is also much decreased within the charge-self-consistent calculation.

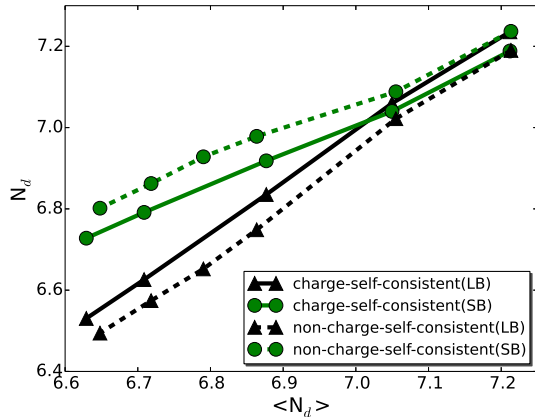


FIG. 11. The d -occupancy, N_d computed for both LB and SB sites in the S3 structure computed using charge-self-consistent DFT+DMFT (solid lines) and non-charge-self-consistent DFT+DMFT (dashed lines) as a function of the average $\langle N_d \rangle$ between two sites.

Here, we fix the U and J values during the DFT+DMFT calculations, therefore the main difference between charge-self-consistent and non-charge-self-consistent results is originated from the change of the Wannier Hamiltonian due to the charge update (see Appendix A). The main role of the charge update is to decrease the crystal field splitting in the S1 and S2 structures and to promote the homogeneous spin-state transition. At the same time, the spin-state and charge ordering effects in the S3 structure has been reduced as the crystal field splitting in the LB site has been increased while it has been decreased in the SB site acting counter-intuitively on the structural effect. Moreover, the overall d -orbital level in the LB site is substantially lowered than the level in the SB site due to the charge update, again decreasing the charge ordering effect. Therefore, the charge-self-consistent effect compensates for the spin-state and charge ordering effects in the S3 structure while it favors the homogeneous spin-state transition, and as a result, the energy difference between the spin-state ordering and the homogeneous spin state has been much reduced within the charge-self-consistent DFT+DMFT calculations.

IV. CONCLUSION

In conclusion, we adopt the charge-self-consistent DFT+DMFT method to study the nature and energetics of both homogeneous and MS states in covalent LaCoO_3 . We find that structural changes during the spin-state transition are important to understand both energetics and electronic structure in LaCoO_3 . As the crystal volume is expanded, the occupation probability of higher spin state in a Co ion increases and a sharp and narrow peak in the imaginary part of the self-energy develops

outside the Co-O hybridization gap due to the enhanced electron correlation. This paramagnetic insulating state also exhibit a multi-configurational mixture of both HS and LS states with strong spin and charge fluctuations. This DMFT result is different from the static DFT+U result showing various meta-stable solutions. The MS state in the BD structure accompanies the HS state in a LB Co site and the LS state in a SB site. Charge ordering is also induced from this spin-state ordering since HS favors the d^6 charge state while LS occupies more d^7 states as covalently bonded with O ions. The LB site with HS becomes a Mott insulator while the SB site with LS behaves as a band insulator. Our DFT+DMFT calculation reveals that energetics between homogeneous and MS states are very close while DFT+U energetics depend sensitively on spin-states and structures favoring the MS state.

We also find that the Co-O covalency plays a crucial role in electronic structure of LaCoO_3 . Changing the double-counting potential in DFT+DMFT can lead to a different N_d value tuning the covalency effectively and both energetics and one-particle spectra are more consistent with experiments when $N_d \sim 6.7$. Increasing the Co-O covalency produces the insulator-to-metal transition favoring the LS state. Increasing temperature beyond 500K also reduces the correlation effect and drives the insulator-to-metal transition, similarly as the experiment. The charge-self-consistency effect within DFT+DMFT reduces the tendency toward spin-state and charge orderings in LaCoO_3 producing close energetics between different structures compared to the non-charge-self-consistent calculation.

ACKNOWLEDGMENTS

H. Park acknowledges helpful discussions with Andrew Millis. H. Park and R. Nanguneri are supported by the U.S. Department of Energy (DOE), Office of Science, Basic Energy Sciences (BES), Materials Sciences and Engineering Division. A. Ngo is supported by the Vehicle Technologies Office (VTO), Department of Energy (DOE), USA. We also gratefully acknowledge the computing resources provided on Bebop, a high-performance computing cluster operated by the Laboratory Computing Resource Center at Argonne National Laboratory.

APPENDIX A: THE d -ORBITAL HAMILTONIAN

In this Appendix, we show the matrix elements of the multi-orbital Hamiltonian, \hat{H}^{dd} , in the Co $3d$ shell at each correlated site for three structures (S1, S2, S3 LB, and S3 SB) used in the DFT+DMFT calculations of this paper. First, we provide \hat{H}^{dd} (in units of eV) represented using MLWF d -orbitals obtained from the DFT solution, which is relevant to the non-charge-self-consistent

DFT+DMFT calculation. The orbital order representing \hat{H}^{dd} is $d^{3z^2-r^2}$, d^{xz} , d^{yz} , $d^{x^2-y^2}$, and d^{xy} .

$$\hat{H}_{S1}^{dd} = \begin{pmatrix} 6.912 & 0.006 & -0.05 & -0.00 & -0.01 \\ 0.006 & 6.236 & 0.019 & -0.01 & -0.02 \\ -0.05 & 0.019 & 6.241 & -0.02 & -0.02 \\ -0.00 & -0.01 & -0.02 & 6.917 & -0.01 \\ -0.01 & -0.02 & -0.02 & -0.01 & 6.237 \end{pmatrix} \quad (4)$$

$$\hat{H}_{S2}^{dd} = \begin{pmatrix} 6.575 & -0.01 & -0.050 & -0.00 & 0.009 \\ -0.01 & 5.948 & -0.02 & 0.013 & -0.02 \\ -0.050 & -0.02 & 5.954 & -0.02 & 0.020 \\ -0.00 & 0.013 & -0.02 & 6.579 & 0.010 \\ 0.009 & -0.02 & 0.020 & 0.010 & 5.949 \end{pmatrix} \quad (5)$$

$$\hat{H}_{S3,LB}^{dd} = \begin{pmatrix} 6.484 & 0.003 & 0.054 & -0.00 & 0.005 \\ 0.003 & 5.913 & -0.02 & -0.00 & 0.018 \\ 0.054 & -0.02 & 5.921 & 0.027 & -0.02 \\ -0.00 & -0.00 & 0.027 & 6.489 & 0.002 \\ 0.005 & 0.018 & -0.02 & 0.002 & 5.915 \end{pmatrix} \quad (6)$$

$$\hat{H}_{S3,SB}^{dd} = \begin{pmatrix} 6.583 & 0.006 & 0.049 & -0.00 & 0.014 \\ 0.006 & 5.909 & -0.02 & -0.02 & 0.022 \\ 0.049 & -0.02 & 5.914 & 0.013 & -0.02 \\ -0.00 & -0.02 & 0.013 & 6.587 & 0.012 \\ 0.014 & 0.022 & -0.02 & 0.012 & 5.910 \end{pmatrix} \quad (7)$$

$$\hat{H}_{S1}^{dd} = \begin{pmatrix} 4.332 & -0.01 & -0.01 & -0.00 & 0.014 \\ -0.01 & 3.737 & -0.01 & 0.022 & 0.006 \\ -0.01 & -0.01 & 3.737 & -0.02 & 0.004 \\ -0.00 & 0.022 & -0.02 & 4.333 & 0.022 \\ 0.014 & 0.006 & 0.004 & 0.022 & 3.735 \end{pmatrix} \quad (8)$$

$$\hat{H}_{S2}^{dd} = \begin{pmatrix} 3.767 & 0.013 & -0.01 & -0.00 & -0.02 \\ 0.013 & 3.158 & 0.006 & -0.02 & 0.007 \\ -0.01 & 0.006 & 3.157 & -0.02 & -0.01 \\ -0.00 & -0.02 & -0.02 & 3.767 & -0.02 \\ -0.02 & 0.007 & -0.01 & -0.02 & 3.156 \end{pmatrix} \quad (9)$$

$$\hat{H}_{S3,LB}^{dd} = \begin{pmatrix} 3.150 & -0.02 & 0.016 & -0.00 & -0.02 \\ -0.02 & 2.490 & 0.009 & 0.037 & -0.01 \\ 0.02 & 0.009 & 2.488 & 0.033 & 0.006 \\ -0.00 & 0.037 & 0.033 & 3.148 & -0.04 \\ -0.02 & -0.01 & 0.006 & -0.04 & 2.487 \end{pmatrix} \quad (10)$$

$$\hat{H}_{S3,SB}^{dd} = \begin{pmatrix} 4.519 & -0.01 & 0.006 & -0.00 & -0.01 \\ -0.01 & 3.984 & 0.006 & 0.017 & -0.01 \\ 0.006 & 0.006 & 3.984 & 0.014 & 0.005 \\ -0.00 & 0.017 & 0.014 & 4.520 & -0.02 \\ -0.01 & -0.01 & 0.005 & -0.02 & 3.983 \end{pmatrix} \quad (11)$$

APPENDIX B: DOUBLE COUNTING CORRECTION

First of all, the local axis for initial projections of MLWFs are chosen to be aligned to the Co-O octahedron axis, therefore the off-diagonal elements are close to zeros. The crystal-field splittings between e_g and t_{2g} orbitals are $\sim 0.67\text{eV}$ for S1, $\sim 0.63\text{eV}$ for S2, $\sim 0.57\text{eV}$ for S3 LB, and $\sim 0.68\text{eV}$ for S3 SB. As expected, the Co-O bond length can tune the crystal-field splitting (the energy difference between e_g and t_{2g} orbitals). Namely, the long-bond Co ion has the smaller splitting and favors higher spin-states.

The charge-self-consistency effect in DFT+DMFT produces a new charge density ρ which is different from the original DFT ρ . As a result, \hat{H}^{dd} is computed from the updated ρ and is also changed. Here, we show below \hat{H}^{dd} obtained from charge-self-consistent DFT+DMFT calculations using $U=6\text{eV}$, $J=0.9\text{eV}$, and the DC parameter $\alpha=0.6$. In this case, the crystal-field splittings are $\sim 0.6\text{eV}$ for S1 and S2, $\sim 0.66\text{eV}$ for S3 LB, and $\sim 0.54\text{eV}$ for S3 SB. The main effect of the charge-self-consistency on \hat{H}^{dd} is to reduce the crystal-field splittings for S1 and S2 structures compared to the non-charge-self-consistency case, therefore it promotes the homogeneous spin-state transition. However, the charge-self-consistency effect also compensates for the spin-state and charge orderings as the crystal-field splitting has been increased for the LB site while it is decreased for the SB site in the S3 structure. The average d -orbital level for the LB site becomes also much lower than the SB site, again compensating for charge ordering.

A frequently used expression of the double-counting energy E^{DC} is the fully localized limit (FLL) form⁴⁸ which has been adopted frequently in DFT+U.

$$E^{DC} = \frac{U}{2} \cdot N_d \cdot (N_d - 1) - \frac{J}{4} \cdot N_d \cdot (N_d - 2) \quad (12)$$

$$V^{DC} = \frac{\partial E^{DC}}{\partial N_d} = U \cdot (N_d - \frac{1}{2}) - \frac{J}{2} \cdot (N_d - 1) \quad (13)$$

where N_d is the occupancy of the correlated site and can be obtained as the result of self-consistent DFT+DMFT or DFT+U calculations. Therefore, the V^{DC} potential depends on the correlated site since N_d is site-dependent.

Recently, it has been shown that the exact form of V^{DC} within DFT+DMFT⁵³ can be computed and the formulae should be close to the nominal DC form, where N_d in Eq. 13 is replaced to the nominal d -occupancy in the atomic limit, N_d^0 , which is site-independent.

$$V^{DC} = U \cdot (N_d^0 - \frac{1}{2}) - \frac{J}{2} \cdot (N_d^0 - 1) \quad (14)$$

The hybridization of d and p orbitals in transition metal oxides means that the resulting d -occupancy N_d will be larger than the nominal value N_d^0 ($N_d > N_d^0$), therefore the nominal V^{DC} will be always smaller than the FLL V^{DC} . This smaller V^{DC} potential reduces the covalency effect between d and p orbitals.

In this paper, we use the following forms of E^{DC} and V^{DC} by modifying the FLL forms to allow the tuning of V^{DC} for changing the Co-O covalency effect.

$$E^{DC} = \frac{U}{2} \cdot \overline{N}_d \cdot (\overline{N}_d - 1) - \frac{J}{4} \cdot \overline{N}_d \cdot (\overline{N}_d - 2) \quad (15)$$

$$V^{DC} = U \cdot (\overline{N}_d - \frac{1}{2}) - \frac{J}{2} \cdot (\overline{N}_d - 1) \quad (16)$$

where $\overline{N}_d = N_d - \alpha$ with a parameter α . Our V^{DC} formula can be derived from E^{DC} ($V^{DC} = \partial E^{DC} / \partial N_d$) and allow site-dependent potentials similarly as the FLL form. The conventional FLL DC form is recovered by setting $\alpha=0$. By increasing α , V^{DC} can be close to the nominal V^{DC} value as \overline{N}_d approaches to N_d^0 ($\alpha = N_d -$

N_d^0).

Another modified form of V^{DC} for DFT+DMFT was also suggested as below since the U value used in the FLL form can be smaller than the Hubbard U ($U' < U$) to allow the smaller V^{DC} potential than the FLL one:

$$E^{DC} = \frac{U'}{2} \cdot N_d \cdot (N_d - 1) - \frac{J}{4} \cdot N_d \cdot (N_d - 2) \quad (17)$$

$$V^{DC} = U' \cdot (N_d - \frac{1}{2}) - \frac{J}{2} \cdot (N_d - 1) \quad (18)$$

where $U' = U - \alpha$ with a parameter α . Here, the role of α is the same as the one in Eq. 16. Namely, the covalency effect can be reduced by increasing the α value. It has been shown that using $U' = U - 0.2\text{eV}$ can successfully reproduce the structural and electronic phase diagram of rare-earth nickelates^{42,49}.

-
- ¹ M. Imada, A. Fujimori, and Y. Tokura, *Rev. Mod. Phys.* **70**, 1039 (1998).
- ² N. B. Ivanova, S. G. Ovchinnikov, M. M. Korshunov, I. M. Eremin, and N. V. Kazak, *Physics-Uspekhi* **52**, 789 (2009).
- ³ T. Saitoh, T. Mizokawa, A. Fujimori, M. Abbate, Y. Takeda, and M. Takano, *Phys. Rev. B* **55**, 4257 (1997).
- ⁴ M. Abbate, J. C. Fuggle, A. Fujimori, L. H. Tjeng, C. T. Chen, R. Potze, G. A. Sawatzky, H. Eisaki, and S. Uchida, *Phys. Rev. B* **47**, 16124 (1993).
- ⁵ R. F. Klie, J. C. Zheng, Y. Zhu, M. Varela, J. Wu, and C. Leighton, *Phys. Rev. Lett.* **99**, 047203 (2007).
- ⁶ C. Zobel, M. Kriener, D. Bruns, J. Baier, M. Grüninger, T. Lorenz, P. Reutler, and A. Revcolevschi, *Phys. Rev. B* **66**, 020402(R) (2002).
- ⁷ M. W. Haverkort, Z. Hu, J. C. Cezar, T. Burnus, H. Hartmann, M. Reuther, C. Zobel, T. Lorenz, A. Tanaka, N. B. Brookes, H. H. Hsieh, H.-J. Lin, C. T. Chen, and L. H. Tjeng, *Phys. Rev. Lett.* **97**, 176405 (2006).
- ⁸ A. Podlesnyak, S. Streule, J. Mesot, M. Medarde, E. Pomjakushina, K. Conder, A. Tanaka, M. W. Haverkort, and D. I. Khomskii, *Phys. Rev. Lett.* **97**, 247208 (2006).
- ⁹ P. M. Raccah and J. B. Goodenough, *Phys. Rev.* **155**, 932 (1967).
- ¹⁰ R. A. Bari and J. Sivardière, *Phys. Rev. B* **5**, 4466 (1972).
- ¹¹ M. Sears-Rodríguez and J. Goodenough, *Journal of Solid State Chemistry* **116**, 224 (1995).
- ¹² T. Kyömen, Y. Asaka, and M. Itoh, *Phys. Rev. B* **71**, 024418 (2005).
- ¹³ A. A. Yaroslavl'tsev, M. Izquierdo, R. Carley, M. E. Dávila, A. A. Únal, F. Kronast, A. Lichtenstein, A. Scherz, and S. L. Molodtsov, *Phys. Rev. B* **93**, 155137 (2016).
- ¹⁴ K. Asai, O. Yokokura, N. Nishimori, H. Chou, J. M. Tranquada, G. Shirane, S. Higuchi, Y. Okajima, and K. Kohn, *Phys. Rev. B* **50**, 3025 (1994).
- ¹⁵ K. Berggold, M. Kriener, P. Becker, M. Benomar, M. Reuther, C. Zobel, and T. Lorenz, *Phys. Rev. B* **78**, 134402 (2008).
- ¹⁶ Knížek, K., Jiráček, Z., Hejtmánek, J., Veverka, M., Marysko, M., Maris, G., and Palstra, T. T.M., *Eur. Phys. J. B* **47**, 213 (2005).
- ¹⁷ P. G. Radaelli and S.-W. Cheong, *Phys. Rev. B* **66**, 094408 (2002).
- ¹⁸ J.-Q. Yan, J.-S. Zhou, and J. B. Goodenough, *Phys. Rev. B* **69**, 134409 (2004).
- ¹⁹ V. Gnezdilov, V. Fomin, A. V. Yermenko, K.-Y. Choi, Y. Pashkevich, P. Lemmens, S. Shiryayev, G. Bychkov, and S. Barilo, *Low Temperature Physics* **32**, 162 (2006).
- ²⁰ D. Fuchs, C. Pinta, T. Schwarz, P. Schweiss, P. Nagel, S. Schuppler, R. Schneider, M. Merz, G. Roth, and H. v. Löhneysen, *Phys. Rev. B* **75**, 144402 (2007).
- ²¹ J. W. Freeland, J. X. Ma, and J. Shi, *Applied Physics Letters* **93**, 212501 (2008).
- ²² W. S. Choi, J.-H. Kwon, H. Jeon, J. E. Hamann-Borrero, A. Radi, S. Macke, R. Sutarto, F. He, G. A. Sawatzky, V. Hinkov, M. Kim, and H. N. Lee, *Nano Letters* **12**, 4966 (2012).
- ²³ G. E. Sterbinsky, R. Nangneri, J. X. Ma, J. Shi, E. Karapetrova, J. C. Woicik, H. Park, J.-W. Kim, and P. J. Ryan, *Phys. Rev. Lett.* **120**, 197201 (2018).
- ²⁴ J. Fujioka, Y. Yamasaki, H. Nakao, R. Kumai, Y. Murakami, M. Nakamura, M. Kawasaki, and Y. Tokura, *Phys. Rev. Lett.* **111**, 027206 (2013).
- ²⁵ M. A. Korotin, S. Y. Ezhov, I. V. Solovyev, V. I. Anisimov, D. I. Khomskii, and G. A. Sawatzky, *Phys. Rev. B* **54**, 5309 (1996).
- ²⁶ K. Knížek, P. Novák, and Z. Jiráček, *Phys. Rev. B* **71**, 054420 (2005).
- ²⁷ K. Knížek, Z. Jiráček, J. Hejtmánek, and P. Novák, *Journal of Physics: Condensed Matter* **18**, 3285 (2006).
- ²⁸ K. Knížek, Z. Jiráček, J. Hejtmánek, P. Novák, and W. Ku, *Phys. Rev. B* **79**, 014430 (2009).
- ²⁹ A. Georges, G. Kotliar, W. Krauth, and M. J. Rozenberg, *Rev. Mod. Phys.* **68**, 13 (1996).
- ³⁰ G. Kotliar, S. Y. Savrasov, K. Haule, V. S. Oudovenko, O. Parcollet, and C. A. Marianetti, *Rev. Mod. Phys.* **78**, 865 (2006).
- ³¹ L. Craco and E. Müller-Hartmann, *Phys. Rev. B* **77**, 045130 (2008).
- ³² G. Zhang, E. Gorelov, E. Koch, and E. Pavarini, *Phys. Rev. B* **86**, 184413 (2012).
- ³³ V. Krápek, P. Novák, J. Kuneš, D. Novoselov,

- D. M. Korotin, and V. I. Anisimov, Phys. Rev. B **86**, 195104 (2012).
- ³⁴ B. Chakrabarti, T. Birol, and K. Haule, Phys. Rev. Materials **1**, 064403 (2017).
- ³⁵ J. Kuneš and V. Křápek, Phys. Rev. Lett. **106**, 256401 (2011).
- ³⁶ M. Karolak, M. Izquierdo, S. L. Molodtsov, and A. I. Lichtenstein, Phys. Rev. Lett. **115**, 046401 (2015).
- ³⁷ G. Kresse and J. Hafner, Phys. Rev. B **47**, 558 (1993).
- ³⁸ G. Kresse and J. Hafner, Phys. Rev. B **49**, 14251 (1994).
- ³⁹ G. Kresse and J. Furthmuller, Comput. Mat. Sci. **6**, 15 (1996).
- ⁴⁰ G. Kresse and J. Furthmuller, Phys. Rev. B **54**, 11169 (1996).
- ⁴¹ J. P. Perdew, K. Burke, and M. Ernzerhof, Phys. Rev. Lett. **77**, 3865 (1996).
- ⁴² H. Park, A. J. Millis, and C. A. Marianetti, Phys. Rev. B **90**, 235103 (2014).
- ⁴³ V. Singh, U. Herath, B. Wah, X. Liao, A. H. Romero, and H. Park, arXiv:2002.00068 (2020).
- ⁴⁴ A. A. Mostofi, J. R. Yates, G. Pizzi, Y.-S. Lee, I. Souza, D. Vanderbilt, and N. Marzari, Computer Physics Communications **185**, 2309 (2014).
- ⁴⁵ N. Marzari, A. A. Mostofi, J. R. Yates, I. Souza, and D. Vanderbilt, Rev. Mod. Phys. **84**, 1419 (2012).
- ⁴⁶ K. Haule, Phys. Rev. B **75**, 155113 (2007).
- ⁴⁷ E. Gull, A. J. Millis, A. I. Lichtenstein, A. N. Rubtsov, M. Troyer, and P. Werner, Rev. Mod. Phys. **83**, 349 (2011).
- ⁴⁸ V. I. Anisimov, J. Zaanen, and O. K. Andersen, Phys. Rev. B **44**, 943 (1991).
- ⁴⁹ H. Park, A. J. Millis, and C. A. Marianetti, Phys. Rev. B **89**, 245133 (2014).
- ⁵⁰ K. Haule, T. Birol, and G. Kotliar, Phys. Rev. B **90**, 075136 (2014).
- ⁵¹ X. Wang, M. J. Han, L. de' Medici, H. Park, C. A. Marianetti, and A. J. Millis, Phys. Rev. B **86**, 195136 (2012).
- ⁵² H. T. Dang, A. J. Millis, and C. A. Marianetti, Phys. Rev. B **89**, 161113(R) (2014).
- ⁵³ K. Haule, Phys. Rev. Lett. **115**, 196403 (2015).
- ⁵⁴ H. Park, A. J. Millis, and C. A. Marianetti, Phys. Rev. B **92**, 035146 (2015).
- ⁵⁵ H. Park, A. J. Millis, and C. A. Marianetti, Phys. Rev. Lett. **109**, 156402 (2012).
- ⁵⁶ A. Chainani, M. Mathew, and D. D. Sarma, Phys. Rev. B **46**, 9976 (1992).